

Multi-wavelength spectroscopy of the black hole candidate MAXI J1813–095 during its discovery outburst

M. Armas Padilla,^{1,2*} T. Muñoz-Darias,^{1,2} J. Sánchez-Sierras,² B. De Marco,³
F. Jiménez-Ibarra,^{1,2} J. Casares,^{1,2} J. M. Corral-Santana,⁴ and M. A. P. Torres^{1,2,5}

¹*Instituto de Astrofísica de Canarias (IAC), Vía Láctea s/n, La Laguna 38205, S/C de Tenerife, Spain*

²*Departamento de Astrofísica, Universidad de La Laguna, La Laguna, E-38205, S/C de Tenerife, Spain*

³*Nicolaus Copernicus Astronomical Center, Polish Academy of Sciences, Bartycka 18, PL-00-716 Warsaw, Poland*

⁴*European Southern Observatory (ESO), Alonso de Córdova 3107, Vitacura, Casilla 19, Santiago, Chile*

⁵*SRON, Netherlands Institute for Space Research, Sorbonnelaan 2, 3584 CA, Utrecht, The Netherlands*

Accepted XXX. Received YYY; in original form ZZZ

ABSTRACT

MAXI J1813–095 is an X-ray transient discovered during an outburst in 2018. We report on X-ray and optical observations obtained during this event, which indicate that the source is a new low-mass X-ray binary. The outburst lasted ~ 70 d and peaked at $L_X(0.5\text{--}10\text{keV}) \sim 7.6 \times 10^{36} \text{ erg s}^{-1}$, assuming a distance of 8 kpc. *Swift*/XRT follow-up covering the whole activity period shows that the X-ray emission was always dominated by a hard power-law component with a photon index in the range of 1.4–1.7. These values are consistent with MAXI J1813–095 being in the hard state, in agreement with the ~ 30 per cent fractional root-mean-square amplitude of the fast variability (0.1–50 Hz) inferred from the only *XMM-Newton* observation available. The X-ray spectra are well described by a Comptonization emission component plus a soft, thermal component ($kT \sim 0.2$ keV), which barely contributes to the total flux ($\lesssim 8$ per cent). The Comptonization y -parameter (~ 1.5), together with the low temperature and small contribution of the soft component supports a black hole accretor. We also performed optical spectroscopy using the VLT and GTC telescopes during outburst and quiescence, respectively. In both cases the spectrum lack emission lines typical of X-ray binaries in outburst. Instead, we detect the Ca II triplet and H α in absorption. The absence of velocity shifts between the two epochs, as well as the evolution of the H α equivalent width, strongly suggest that the optical emission is dominated by an interloper, likely a G–K star. This favours a distance $\gtrsim 3$ kpc for the X-ray transient.

Key words: accretion, accretion discs – X-rays: binaries – black hole physics – X-rays: individual: MAXI J1813–095

1 INTRODUCTION

The most extreme stellar compact objects, black holes (BHs) and neutron stars (NSs), are often revealed when they reside in low mass X-ray binary (LMXB) systems. In these interacting binaries, the compact object is accreting material from the outer layers of a (sub-)solar companion star that overflows its Roche lobe. Due to conservation of angular momentum, the in-falling gas forms a disc around the compact object, an accretion disc (Shakura & Sunyaev 1973), which can exceed 10^{6-7} K in its innermost regions, emitting strong X-ray radiation. Depending on their X-ray luminosity (a proxy of the accretion rate) LMXBs behave as persistent or transient sources. The former are persistently

accreting and, consequently, they are always luminous, with $L_X > 10^{36} \text{ erg s}^{-1}$ (but see Armas Padilla et al. 2013b). The latter, on the other hand, combine long quiescent states at low X-ray luminosities ($L_X \sim 10^{30-33} \text{ erg s}^{-1}$) with sporadic outburst events, during which they brighten several orders of magnitude. Over these periods of activity (lasting weeks to months), LMXBs display a well established X-ray phenomenology, exhibiting different X-ray states in which their spectral and timing properties vary following (roughly) the changes in the accretion rate (Miyamoto et al. 1992; Homan et al. 2001; van der Klis 2006; Belloni et al. 2011). In the optical/infrared, active LMXBs are characterised by broad, double-peaked emission lines arising from hot gas orbiting in a Keplerian accretion disc geometry (Smak 1969). These features can sometimes show very complex profiles due to e.g. the presence of outflows (Muñoz-Darias et al. 2016)

* E-mail: m.armaspadilla@iac.es

or changes in the disc opacity (Jiménez-Ibarra et al. 2019; Dubus et al. 2001). Finally, ejection processes in the form of jets are ubiquitously observed in the low energy part of the spectrum, from radio waves to (at least) the near-infrared (e.g. Fender et al. 2004).

Despite of this wealth of information, it is not always straightforward to infer the nature of the compact object since most of the above phenomenology is common to BH and NS systems (Fender & Muñoz-Darias 2016; Charles & Coe 2006). We can securely establish the BH nature when the dynamical mass of the compact object exceeds $\sim 3 M_{\odot}$ (Casares & Jonker 2014), the absolute upper limit for NSs according to General Relativity (Rhoades & Ruffini 1974; Kalogera & Baym 1996). NS systems, on the other hand, are unveiled when events associated to the presence of a hard surface are witnessed. These are thermonuclear X-ray bursts and coherent pulsations. In the absence of any of the above, one relies on either the long-term evolution or a very detailed analysis of the X-ray timing and spectral characteristics. From the spectral point of view, a thermal accretion disc and a hard tail produced by inverse-Compton processes in an optically thin inner flow (corona) are common X-ray spectral components for both NSs and BHs. In addition, NSs possess an extra soft thermal component that arises from the solid surface and/or boundary layer. This component is clearly detected in high signal to noise data of some NS systems (e.g. Armas Padilla et al. 2017). In addition, the latter it is a source of extra seed photons affecting the properties of the Comptonizing Corona, which can be used to constrain the nature of the accretor (Sunyaev & Titarchuk 1989; Burke et al. 2017).

On 2018 February 19 the Monitor of All-sky X-ray Image (MAXI) reported the detection of an uncatalogued X-ray transient, MAXI J1813–095 (Kawase et al. 2018). Following its discovery, the source was monitored by several observatories. Quasi-simultaneous spectra obtained with *Swift* and *INTEGRAL* missions were well modelled by an absorbed powerlaw with photon-index $\Gamma=1.6$ and cutoff energy at ~ 140 keV (Fuerst et al. 2018). The Australia Telescope Compact Array detected the source with a flux density of ~ 0.69 mJy at 5.5 GHz and ~ 0.47 mJy at 9 GHz. This results in a radio spectral index of $\alpha \sim -0.6$, which tentatively points towards a compact jet from a BH in the hard-state (Russell et al. 2018). GROND (Greiner et al. 2008), attached to the MPG 2.2m telescope at the ESO La Silla Observatory (Chile), detected a candidate optical counterpart at $i=18.6$ [RA(J2000) = $18^{\text{h}}13^{\text{m}}34^{\text{s}}.015$, Dec. (J2000) = $-09^{\circ}31'59''20$] which had brightened by 1 magnitude with respect to Pan-STARRS1 (PS1) pre-outburst observations (Rau 2018).

Here, we present a multi-wavelength study of the discovery outburst of MAXI J1813–095. This includes X-ray spectral and temporal analysis from *XMM-Newton* and *Swift* as well as optical spectroscopy taken with the Very Large Telescope (VLT) during outburst and the Gran Telescopio Canarias (GTC) in quiescence.

2 OBSERVATIONS AND DATA REDUCTION

2.1 *Swift* data

The Neil Gehrels *Swift* Observatory (Gehrels et al. 2004) pointed to MAXI J1813–095 on 11 occasions with the on-

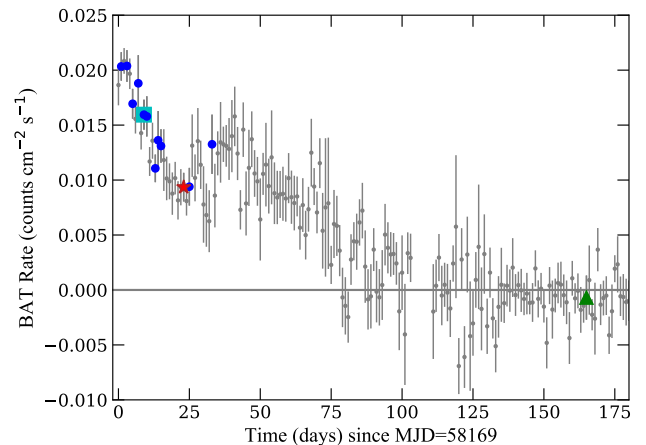


Figure 1. The 2018 outburst light curve (15–50 keV) of MAXI J1813–095 obtained by *Swift*/BAT. The dates of the *Swift*/XRT and *XMM-Newton* observations are indicated by blue circles and a red star, respectively. A cyan square (VLT) and a green triangle (GTC) indicate the epochs of our optical spectroscopy.

board X-ray Telescope (XRT; Burrows et al. 2005) operated in window timing (WT) mode (see Fig 1 and Table 1 for the observing log). We used the *HEASoft* v.6.20 package to reduce the data. We processed the raw XRT data running the *xrtpipeline* task selecting the standard event grades of 0-2. We extracted (using *Xselect* v2.4) the source spectra, light curves and images from a circular region of ~ 60 arcsec (25 pixels) radius. To compute the background, we used an annulus centred on the source with an 180 arcsec (75 pixels) inner radius and 300 arcsec (125 pixels) outer radius. We created exposure maps and ancillary response files following the standard *Swift* analysis threads¹, and acquired the last version of the response matrix files from the High Energy Astrophysics Science Archive Research Center calibration database. In order to be able to use χ^2 statistics consistently, the spectral data were grouped in bins containing a minimum of 20 photons.

2.2 *XMM-Newton* data

XMM-Newton (Jansen et al. 2001) observed MAXI J1813–095 during 26.7 ksec on 2018 March 15 (ID 0830190101). During the trigger, the European Photon Imaging Camera (EPIC) was operated with the thin filter in the small-window imaging mode, in the case of MOS1 camera, and the timing mode for MOS2 and PN cameras (Turner et al. 2001, Strüder et al. 2001). We used the Science Analysis Software (SAS, v.16.0.0) to obtain calibrated events and scientific products.

We excluded events with high background flaring activity by filtering the periods with count rates larger than $0.3 \text{ counts s}^{-1}$ (> 10 keV) and $0.7 \text{ counts s}^{-1}$ (10–12 keV) for the MOS1 and PN cameras, respectively. MOS1 source events have a count rate of $\sim 17 \text{ counts s}^{-1}$, well beyond the threshold of $\sim 5 \text{ counts s}^{-1}$ where pile up starts to be an issue in the small-window mode. We confirmed this by using

¹ <http://www.swift.ac.uk/analysis/xrt/>

the pile up evaluation tool EPATPLOT. In order to mitigate pile up effects we used an annulus region excluding a large central portion (15 arcsec inner radius and a 40 arcsec outer radius) to extract the source filtered events. This resulted in a low statistic spectrum and, therefore, we did not include MOS1 data in our study. We also excluded MOS2 data from our analysis because of the calibration uncertainties in the MOS cameras in the timing mode ².

We extracted PN source and background events from the RAWX columns in [30:44] and in [6:14], respectively. The source count rate is ~ 60 counts s^{-1} , which is much lower than the 800 counts s^{-1} pile-up threshold. We generate the light curves, spectra, associated response matrix files (RMFs) and ARFs following the standard analysis threads ³.

The source was detected by the Reflection Grating Spectrometer (RGS) which was operated in the standard spectroscopy mode. We used the SAS task RGSPROC to reduce the RGS data and to produce the response matrices and spectra. We included the RGS1 and RGS2 first order spectra in our analysis.

We rebinned the spectra in order to include a minimum of 25 counts in every spectral channel, avoiding to oversample the full width at half-maximum of the energy resolution by a factor larger than 3.

2.3 Optical observations

We carried out optical spectroscopy of MAXI J1813–095 at two different epochs: close to the (observed) peak of the outburst and ~ 150 d later, when the source was no longer detected by X-ray monitors and was expected to be near its quiescent level (Fig. 1). Outburst observations were carried on March 1, 2018 using the instrument X-shooter (Vernet et al. 2011) attached to the VLT-UT2 telescope in Cerro Paranal, Chile. This instrument has 3 different arms covering the ultraviolet, visible and near-infrared spectral ranges. The source was not detected in the ultraviolet due to the strong reddening, while the low signal-to-noise achieved in the infrared prevented us from carrying out an adequate telluric correction. Therefore, we use only data from the visible X-Shooter arm in this paper. We obtained two exposures of 1205 seconds each, that were processed and combined using version 3.2.0 of the X-shooter pipeline. Observations were obtained under clear conditions and a seeing of ~ 0.6 arcsec, while a slit-width of 0.9 arcsec was used. This combined with a 2×2 binning rendered a velocity resolution of ~ 35 km s^{-1} .

We observed again MAXI J1813–095 using the Optical System for Imaging and low-Intermediate Resolution Integrated Spectroscopy (OSIRIS; Cepa et al. 2000) attached to the GTC at the Observatorio del Roque de Los Muchachos located in La Palma, Spain. Observations took place under clear conditions on August 3, 2018. We used the grism R2500R ($1.04 \text{ \AA pix}^{-1}$), which covers the spectral range 5575–7685 \AA . We took one spectrum of 1800 s using a slit-width of 0.8 arcsec, which provided a spectral resolution of 137 km s^{-1} (measured as the full-width at half-maximum of a sky line at $\sim 6300 \text{ \AA}$). We reduced the data and extracted the

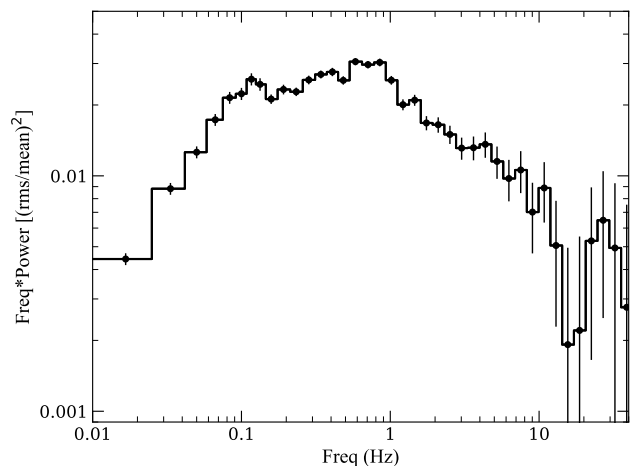


Figure 2. The PSD of MAXI J1813–095 in the 1–10 keV energy band. It is displayed Poisson noise-subtracted and using the fractional root-mean-square normalization (Miyamoto et al. 1991).

spectrum using IRAF standard routines and custom PYTHON software. We used sky emission lines and the MOLLY software to measure and correct subpixel velocity drifts of ~ 24 km s^{-1} introduced by flexure effects.

For both the VLT and GTC observations we obtained photometric measurements from the acquisition images. These were reduced in the standard way using ASTROPY-CCDPROC based routines (Robitaille et al. 2013; Price-Whelan et al. 2018). Aperture photometry was calibrated against nearby stars present in the PS1 catalog (Chambers et al. 2016). We obtained *i*-band magnitudes of 18.62 ± 0.02 and 19.43 ± 0.03 , respectively. The former is consistent with the outburst value reported by Rau (2018), while the latter is slightly brighter than the pre-outburst PS1 magnitude ($i = 19.67 \pm 0.03$).

3 ANALYSIS AND RESULTS

3.1 X-ray analysis

We used XSPEC (v.12.9.1; Arnaud 1996) to analyse the X-ray spectra. In order to account for interstellar absorption, we used the Tuebingen-Boulder Interstellar Medium absorption model (TBABS in XSPEC) with cross-sections of Verner et al. (1996) and abundances of Wilms et al. (2000). In this work we assume a distance of 8 kpc (Russell et al. 2018) and an orbital inclination of 60° .

3.1.1 XMM-Newton temporal analysis

EPIC PN light curves in the energy band 1–10 keV were extracted with a time bin of 6 ms. We computed the power spectral density function (PSD) by averaging estimates obtained from segments of 60 s length. The Poisson noise level was estimated by fitting a constant model at frequencies > 30 Hz, where variability associated with counting noise dominates. Fig. 2 shows the resulting Poisson noise-subtracted PSD, with fractional root-mean-square (rms) normalization (Miyamoto et al. 1991). A flat-topped broad

² See the calibration technical note XMM-SOC-CAL-TN-0018

³ <https://www.cosmos.esa.int/web/xmm-newton/sas-threads>

Table 1. Results from *Swift* spectral fits with an absorbed power-law model in which N_{H} was fixed to $1.1 \times 10^{22} \text{ cm}^{-2}$. Quoted errors represent 90% confidence levels.

Obs ID	Date	Exposure(ks)	Γ	$F_{\text{X,unabs}}^{\text{a}}$ (2–10 keV)	L_{X}^{b}	$F_{\text{X,unabs}}^{\text{a}}$ (0.5–10 keV)	L_{X}^{b}	χ^2_{ν} (dof)
00010563002	2018-02-21	0.97	1.53 ± 0.04	5.9 ± 0.2	4.5 ± 0.1	8.4 ± 0.2	6.4 ± 0.1	1.00 (288)
00010563003	2018-02-23	0.83	1.48 ± 0.05	7.1 ± 0.3	5.5 ± 0.2	9.9 ± 0.3	7.6 ± 0.2	1.33 (174)
00010563004	2018-02-25	0.41	1.63 ± 0.05	6.3 ± 0.3	4.8 ± 0.2	9.4 ± 0.3	7.2 ± 0.2	0.94 (189)
00088654001	2018-02-27	1.8	1.53 ± 0.02	5.7 ± 0.1	4.4 ± 0.1	8.1 ± 0.1	6.2 ± 0.1	1.13 (496)
00010563005	2018-03-01	0.48	1.50 ± 0.05	5.1 ± 0.2	3.9 ± 0.2	7.1 ± 0.2	5.5 ± 0.2	1.27 (165)
00010563006	2018-03-02	0.90	1.57 ± 0.04	5.0 ± 0.2	3.8 ± 0.1	7.2 ± 0.1	5.5 ± 0.1	1.10 (286)
00010563007	2018-03-05	0.93	1.58 ± 0.04	4.7 ± 0.1	3.6 ± 0.1	6.9 ± 0.1	4.0 ± 0.1	0.99 (282)
00088654002	2018-03-06	1.8	1.54 ± 0.03	4.5 ± 0.1	3.4 ± 0.1	6.4 ± 0.1	4.9 ± 0.1	1.01 (414)
00088654003	2018-03-07	2.24	1.51 ± 0.03	4.5 ± 0.1	3.5 ± 0.1	6.4 ± 0.1	4.9 ± 0.1	1.00 (468)
00010563008	2018-03-17	0.77	1.53 ± 0.05	3.7 ± 0.1	2.8 ± 0.1	5.2 ± 0.1	4.0 ± 0.1	0.96 (191)
00088654004	2018-03-25	1.48	1.67 ± 0.03	4.8 ± 0.1	3.6 ± 0.1	7.3 ± 0.2	5.6 ± 0.1	0.98 (396)

^a Unabsorbed fluxes in units of $10^{-10} \text{ erg cm}^{-2} \text{ s}^{-1}$.^b Luminosities in units of $10^{36} \text{ erg s}^{-1}$.**Table 2.** Fitting results for the *XMM-Newton* observation. Uncertainties are expressed at 90 per cent confidence level.

Component / Model	DISKBB+NTHCOMP+GAUSS	BB+NTHCOMP+GAUSS	DISKBB+COMPPTS+GAUSS
N_{H} ($\times 10^{22} \text{ cm}^{-2}$)	1.08 ± 0.07	1.03 ± 0.05	1.14 ± 0.07
kT_{in} (keV)	0.23 ± 0.03	0.18 ± 0.01	0.21 ± 0.03
$N_{\text{in}/\text{bb}} / R_{\text{in}/\text{bb}}$ (km)	$1222^{+2686}_{-709} / 80^{+63}_{-29}$	$2915^{+3197}_{-1596} / 43^{+19}_{-14}$	$2633^{+5522}_{-1902} / 117^{+89}_{-56}$
Γ / y	$1.55^{+0.04}_{-0.01}$	1.54 ± 0.02	1.5 ± 0.1
kT_{e} (keV)	50 (fix)	50 (fix)	50 (fix)
Refl	–	–	$0.31^{+0.34}_{-0.25}$
$N_{\text{nthcomp}/\text{comppts}}$ ($\times 10^{-2}$)	6.14 ± 0.4	5.8 ± 0.3	3537^{+2334}_{-1586}
E_{gaus} (keV)	$6.7^{+0.4}_{-0.2}$	$6.7^{+0.3}_{-0.2}$	$7.1^{+0.4}_{-0.3}$
σ_{gaus} (keV)	$0.68^{+1.7}_{-0.2}$	$0.67^{+0.7}_{-0.3}$	$1.16^{+1.3}_{-0.4}$
k_{gaus} ($\times 10^{-4} \text{ photons cm}^{-2} \text{ s}^{-1}$)	2.5^{+7}_{-1}	2.5^{+4}_{-1}	3.9^{+15}_{-2}
χ^2 (dof)	541.81 (505)	546.83 (505)	542.72 (504)
(0.5–10 keV)			
$F_{\text{X,unabs}}$ ($\times 10^{-10} \text{ erg cm}^{-2} \text{ s}^{-1}$)	5.1 ± 0.2	4.87 ± 0.1	5.3 ± 0.2
L_{X}^{a} ($\times 10^{36} \text{ erg s}^{-1}$)	3.9 ± 0.2	3.73	4.0 ± 0.2
Thermal fraction ^b (%)	8	5	8
(2–10 keV)			
$F_{\text{X,unabs}}$ ($\times 10^{-10} \text{ erg cm}^{-2} \text{ s}^{-1}$)	3.40 ± 0.01	3.38 ± 0.01	3.4 ± 0.02
L_{X}^{a} ($\times 10^{36} \text{ erg s}^{-1}$)	2.6 ± 0.007	2.59 ± 0.007	2.6 ± 0.02
Thermal fraction ^c (%)	1	< 1	2

^a Unabsorbed luminosity assuming a distance of 8 kpc.^b Fractional contribution of the thermal component to the total 0.5–10 keV flux.^c Fractional contribution of the thermal component to the total 2–10 keV flux.

band noise distribution is observed, which is typical of X-ray binaries in the hard state. Moreover, we find no evidence of quasi-periodic oscillations (QPOs). This is also true if we increase the signal-to-noise ratio by using shorter segments (e.g. 16s) when computing the PSD. In both BH and NS LXRBS, strong, low-frequency QPOs are typically observed in high luminosity states, mostly close to, or during the transition to/from the soft state (e.g. [Motta et al. 2017](#)). Thus, the lack of QPOs is indicative of a low luminosity hard state. Moreover, the integrated 0.1–50 Hz fractional rms yields 31 ± 1 per cent, again typical of low luminosity hard states ([Muñoz-Darias et al. 2011, 2014](#)).

3.1.2 *XMM-Newton* spectral analysis

We simultaneously fitted the 0.6–1.8 keV RGS spectra (RGS1 and RGS2 first order) and the 0.7–10 keV EPIC-

PN spectrum with the parameters tied between the three detectors. We added a constant factor (CONSTANT) to the spectral models with a value fixed to 1 for EPIC–PN spectrum and free to vary for the RGS spectra to account for cross-calibration uncertainties between the instruments. We added a 1 per cent systematic error to all instruments to account for uncertainties in the relative calibration between the RGS and EPIC–PN detectors ([Kirsch et al. 2004](#); XMM-SOC-CAL-TN-0052).

In a first attempt, we fitted the spectra with a single absorbed thermally Comptonized continuum model (NTHCOMP in XSPEC; [Zdziarski et al. 1996](#); [Zycki et al. 1999](#)), which is parametrised by an asymptotic power law index (Γ), the corona electron temperature (kT_{e}) and the up-scattered seed photons temperature (kT_{seed}). The kT_{e} temperature generally adopts values higher than 10 keV in the hard state, which is beyond our spectral coverage (0.5–10 keV).

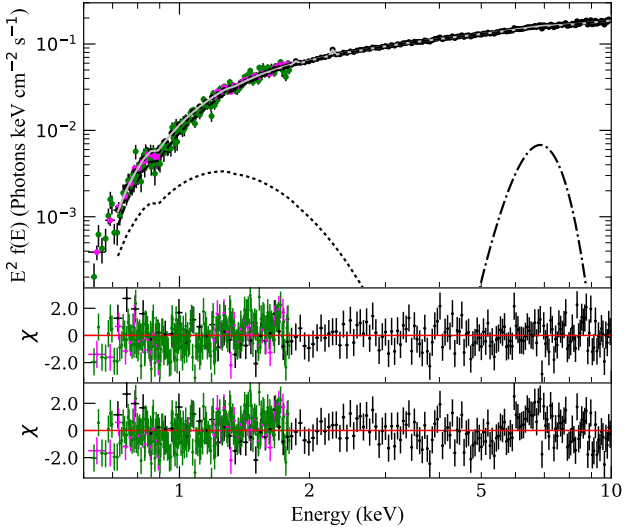


Figure 3. Unfolded PN (black), RGS1 (magenta) and RGS2 (green) spectra and residuals in units of σ when using a DISKBBODY+NTHCOMP+GAUSS model. The full fit is shown as a grey solid line, the black body component as a dotted line, the Comptonized component as a dashed line and the Gaussian component (associated to the Fe $K\alpha$ line) as a dot-dashed line. Bottom panel: Residuals in units of σ for a DISKBBODY+NTHCOMP model (i.e., no Gaussian component).

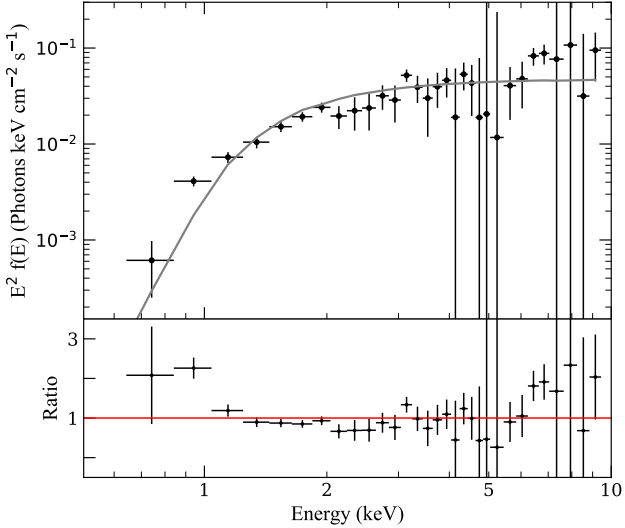


Figure 4. Upper panel: rms-scaled energy spectrum (0.1–50 Hz) derived from the *XMM-Newton* data. Bottom panel: Data-to-model ratio obtained by fitting the rms-scaled spectrum with TBABS*NTHCOMP model (grey solid line).

Hence, we fixed this parameter to the reported e-folding energy of exponential rolloff obtained with *INTEGRAL* spectra (Fuerst et al. 2018). This is $kT_e=50$ keV assuming a relation $E_c = 140 \text{ keV} \approx 3kT_e$ ⁴. However, with a χ^2 of 636.9 for 509 degrees of freedom (dof) the model returned a non

⁴ The actual value of kT_e is within 30–90 keV (since $E_c =$

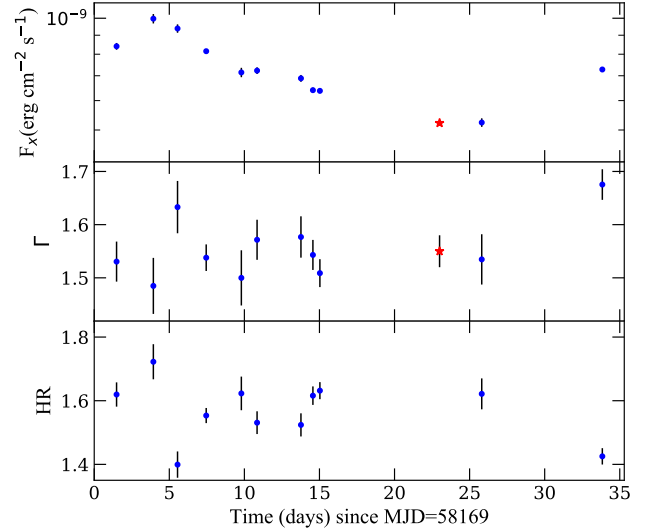


Figure 5. From top to bottom, evolution with time of unabsorbed flux, photon index and hardness ratio (ratio of counts in the 2–10 keV and 0.5–2 keV energy bands). Fluxes are computed in the 0.5–10 keV band. *Swift* data are indicated by a blue circle and *XMM-Newton* observation by a red star.

acceptable fit (p-value⁵ of 9×10^{-5}). In addition to a soft excess, the fit residuals showed two emission features at ~ 1.8 and ~ 2.2 keV produced, most likely, by the detector silicon K-edge (1.8 keV) and the mirror AuM-edge (2.3 keV) (Guainazzi et al. 2014). Therefore, from now on, we added two Gaussian components (GAUSS) in all our models to mitigate these instrumental features. Their inclusion to our model did not significantly improve the fit ($\Delta\chi^2=4$).

In a second step, we added to our previous model a thermal soft component, either a multicolour disc (i.e., DISKBB+NTHCOMP; Mitsuda et al. 1984; Makishima et al. 1986) to account for emission from the accretion disc or a single blackbody (i.e., BBODYRAD+NTHCOMP) to account for the emission from the surface/boundary layer in the case of a NS. We assumed that the seed photons arise from the corresponding thermal component. Thus, we coupled kT_{seed} to either kT_{in} or kT_{bb} , respectively, and changed the seed photons shape parameter accordingly (im-type in NTHCOMP). Both models improved significantly the fit ($\chi^2 \approx 577$ for 508 dof, F-test probability $\sim 10^{-12}$), although they still did not reproduce adequately the data (p-value ≈ 0.01). Both fits leave residuals in the region of ~ 6.4 keV consistent with Fe $K\alpha$ emission (see lower panel in Fig.3). Therefore, we included a Gaussian component (GAUSS), which resulted in an acceptable fit (p-value ≈ 0.1). The line converged to a central energy of $E_1 \sim 6.7$ keV and $\sigma_1 \sim 0.7$ keV with an equivalent width (EW) of 75 eV. When assuming soft emission arising from the ac-

140⁺¹²⁰₋₅₀ keV). Fixing it to 50 keV does not affect significantly the resulting spectral parameters.

⁵ The probability value (p-value) represents the probability that the deviations between the data and the model are due to chance alone. In general, a model can be rejected when the p-value is smaller than 0.05.

cretion disc we got an equivalent hydrogen column (N_{H}) of $(1.08 \pm 0.07) \times 10^{22} \text{ cm}^{-2}$. The obtained temperature at the inner disc radius (kT_{in}) is $0.23 \pm 0.03 \text{ keV}$. The normalization can be translated to an apparent inner disc radius of $R_{\text{in}} \sim 80 \text{ km}$ (with Kubota et al. 1998 correction applied). The Comptonization asymptotic power-law photon index (Γ) is 1.55 ± 0.04 . The inferred 0.5–10 keV unabsorbed flux is $(5.1 \pm 0.2) \times 10^{-10} \text{ erg cm}^{-2} \text{ s}^{-1}$, to which the thermal component contributes 8 per cent. Likewise, in the 2–10 keV band, we measure $(3.40 \pm 0.01) \times 10^{-10} \text{ erg cm}^{-2} \text{ s}^{-1}$ and a thermal contribution of 1 per cent. Similar values are recovered for the Comptonizing parameters when using a single blackbody as the soft thermal component (see Table 2). The resulting blackbody temperature was $kT_{\text{bb}} = 0.18 \pm 0.01 \text{ keV}$ with an inferred emission radius of $R_{\text{bb}} = 43_{-14}^{+19} \text{ km}$.

We also tried the three-component model (DISKBB+BBODYRAD+NTHCOMP+GAUSS) proposed for NS hard state spectra when high-quality coverage at low energies is available (Armas Padilla et al. 2017, 2018; see also Lin et al. 2007). The model adequately fits the spectra ($\chi^2 \approx 540$ for 503 dof), but the extra thermal component is not statistically required (F-test probability > 0.1).

With the aim of comparing with literature, in particular with the work of Burke et al. (2017), we also modelled the Comptonised emission using the COMPPS model (Poutanen & Svensson 1996). Following this work we used the model DISKBB+COMPPS+GAUSS with the same parameter constraints (section 3 and 5.5 of Burke et al. 2017). This model returned consistent values for N_{H} , the thermal component and the fluxes (see Table 2). With regards to the Comptonizing component, the y -parameter (y) obtained is ~ 1.5 and the reflection strength ($R = \Omega/2\pi$) ~ 0.3 . The resulting line central energy is slightly higher ($E_1 \sim 7.1 \text{ keV}$ and $\sigma_1 \sim 1.2 \text{ keV}$) than that derived above, probably due to coupling with the Fe edge (7.1 keV) of the reflection continuum. In fact, if we fix the reflection strength to zero, the Gaussian parameters converge to similar values than those obtained with NTHCOMP.

3.1.3 Spectral-timing analysis

In the last two decades significant efforts have been dedicated to study the effects of the different spectral components in the time domain (e.g. Gilfanov et al. 2000, Yamada et al. 2013). With this aim, we computed the fractional-rms as a function of the energy (rms spectrum) using the *XMM-Newton* PN data and following for every energy bin the procedure described in Sec 3.1.1. This resulted in a flat rms spectrum, which is typical of BHs in the hard state (see e.g. fig. 4 in Belloni et al. 2011). Subsequently, we used this rms spectrum to rescale the energy spectrum, which yielded the rms-scaled energy spectrum (e.g. Uttley et al. 2014). It shows the spectral shape of the components contributing to the observed variability over a given time scale (0.1–50 Hz in this case). Given the shape of the PSD (Fig. 2) this frequency band encompasses almost all the observed X-ray variability. The rms-scaled spectrum is shown in Fig. 4 together with the data-to-model ratio obtained after fitting it with a thermal comptonization model [TBABS*NTHCOMP in Xspec with N_{H} fixed to that derived from the regular spectral fits (Sect. 3.1.2)]. The fit reveals clear excess residuals (bottom

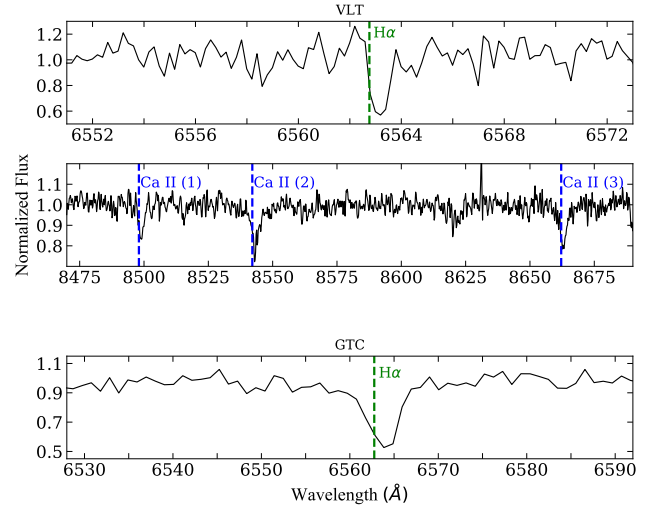


Figure 6. Two top panels: VLT/X-shooter spectrum taken during outburst. The H_{α} (green) and CaII Triplet (blue) absorptions are marked with dotted lines. Bottom panel: GTC/OSIRIS spectrum in the H_{α} region taken during quiescence.

panel) at low energies ($E \lesssim 2 \text{ keV}$), suggesting the presence of significant variability associated with the soft component (i.e. the DISKBB component; see Fig. 3). This residual is also significantly detected when splitting the variability over long (0.1–1 Hz) and short (1–50 Hz) time scales.

We note that additional residuals are seen at the energy of the Fe line. Adding a Gaussian component yields a centroid energy of $\sim 6.6 \text{ keV}$, consistent with the laboratory energy of the line. However, this feature is not significant in the rms-scaled spectrum ($\Delta\chi^2 = 2$ for 3 dof).

3.1.4 Swift analysis

All *Swift* spectra are well described by an absorbed power-law model, in which we fixed the N_{H} to the value obtained from the *XMM-Newton* fit ($N_{\text{H}} = 1.1 \times 10^{22} \text{ cm}^{-2}$). Results are reported in Table 1 and Fig 5. Across the 34 d *Swift*/XRT monitoring, Γ fluctuated in the range of ~ 1.45 – 1.70 and the 0.5–10 keV unabsorbed flux varied by a factor of 2. The flux peaked on February 23 with a value of $(9.9 \pm 0.3) \times 10^{-10} \text{ erg cm}^{-2} \text{ s}^{-1}$ and smoothly decreased to a $(5.2 \pm 0.2) \times 10^{-10} \text{ erg cm}^{-2} \text{ s}^{-1}$ over the following 27 days. On March 25 there was a small re-brightening after which the source returned to quiescence (see Fig 1). Assuming a distance of 8 kpc, the above correspond to a luminosity range of $(4 - 7.6) \times 10^{36} \text{ erg s}^{-1}$. The Harness Ratio (HR; ratio of counts in the 2–10 keV and 0.5–2 keV energy bands) oscillates in the range of ~ 1.4 – 1.6 . These values indicate that the source remained in the hard state during the full outburst and are fully consistent with the *XMM-Newton* timing and spectral results.

3.2 Optical spectroscopy

The outburst VLT spectrum is shown in the upper panels of Fig. 6. The strongest features detected correspond to the Ca II triplet at 8500–8600 Å. These absorption lines do

not typically arise from accretion discs but from stars with spectral types later than F. However, in M stars these are accompanied by very broad absorption components of different elements not present in our data, while early F stars show also weak Paschen transitions on the red wing of the Ca II absorptions. In addition, we detect weaker absorption of Mg I at 8806.8 Å (not shown), also typical of late spectral type stars. All the above suggests that the outburst optical spectrum is dominated by the emission from a G–K star.

Unfortunately, the quiescent spectrum (GTC) did not cover the Ca II triplet region. Instead, we clearly detected H α in absorption with an equivalent width of 2.7 ± 0.2 Å. A Gaussian fit to this line reveals that it is shifted by 40 ± 5 km s $^{-1}$ with respect to the laboratory wavelength. The same technique applied to the Ca II triplet (i.e. multi-Gaussian fit) and Mg I detected in outburst yields a velocity offset of 36 ± 1 km s $^{-1}$, that is, consistent with the quiescence value. Unless both observations were taken (by chance) at the same orbital phase or the orbital inclination is (very) close to zero, the above suggests that the absorption lines arise from a field, interloper star (i.e. not from the donor star).

A careful inspection of the outburst spectrum also reveals a weak H α absorption, in this case with an equivalent width of 0.33 ± 0.05 Å (see top panel in Fig 6). The line is centred at $+17$ km s $^{-1}$, slightly (but significantly) different than both the Ca II triplet velocity derived from the same spectrum and that of H α itself measured in quiescence. This can be explained if the emission from the interloper is veiled by the actual optical emission from the accretion disc during outburst. Indeed, this extra emission must be present in order to account for the ~ 0.8 mag brightening that we determined from the acquisition images. It is also expected to include additional H α emission (but not Ca II), since this is the strongest emission line typically detected in LMXBs in outburst (Mata Sánchez et al. 2018). Interestingly, a rise of ~ 0.8 mag in the continuum from quiescence to outburst, would imply a drop in the equivalent width by a factor of 2.1 (i.e., $2.7/2.1 = 1.3$ Å would be expected in outburst). Since we measure an equivalent width of ~ 0.3 Å this suggests that the absorption is indeed filled by extra emission. The latter might account for the different velocity offset as it is likely centred at a different systemic velocity than that of the interloper.

4 DISCUSSION

In this work, we report on the X-ray and optical spectroscopic observations as well as the long-term evolution of MAXI J1813–095 during its discovery outburst. The X-ray spectral properties, the outburst intensity and duration, and the temporal properties, indicate that MAXI J1813–095 is a new member of the family of LMXBs.

According to the *Swift*/BAT light curve (Fig. 1) the duration of the outburst was ~ 75 d with the first detection on February 19, 2018 (we notice that the source was not observable before February 14 due to Sun-constraints). If we assume a distance of 8 kpc, we obtain a 0.5–10 keV peak luminosity of 7.6×10^{36} erg s $^{-1}$. The integrated fractional rms inferred from the *XMM-Newton* data is ~ 31 per cent (0.1–50 Hz), which indicates that the source was in the hard state at that time (Muñoz-Darias et al. 2011, 2014). Fur-

thermore, the photon index values are in the range of ~ 1.4 – 1.7 along the whole outburst, which strongly suggests that the source never transitioned to the soft state (McClintock & Remillard 2006; Done et al. 2007) and remained in the hard state during the event. This behaviour is not unheard in the family of LMXBs. Indeed, sources always showing only hard state outburst as well as systems typically displaying regular outburst with occasional (typically fainter) only hard state events (a.k.a. failed outburst) have been observed (e.g. Capitanio et al. 2009; Motta et al. 2010; Armas Padilla et al. 2013a; Koljonen et al. 2016; Muñoz-Darias et al. 2014).

In the absence of dynamical measurements, thermonuclear X-ray bursts and coherent pulsations, the spectral characteristics can help to infer the nature of the compact object. However, we have been able to model the *XMM-Newton* spectra by using both BH-like and NS-like models. Therefore, we have to scrutinize the obtained parameters in order to make an attempt to tag the accretor class. Two of the most revealing model parameters are related to the Comptonizing Corona. These are the electron temperature and optical depth, which combine in the so-called Compton y -parameter⁶. This was best showed in Burke et al. (2017), who found a dichotomy between the Comptonization properties of BH and NS systems while in the hard state. In particular, they found a boundary at $y \approx 0.9$, with NSs sitting below this value and BHs above it. The difference implies that in a Corona with a given optical depth, the temperature will be lower for NS systems, which supports the idea that the properties of the Comptonizing Corona are affected by the additional seed photons coming from the NS (Sunyaev & Titarchuk 1989). In fact, Burke et al. (2017) found that while the electron temperature kT_e in BH systems can cover a broad range, from $kT_e \sim 30$ to 200 keV, kT_e peaks at ~ 15 – 25 keV for NSs, with very few spectra exceeding $kT_e \sim 50$ – 70 keV. In the case of MAXI J1813–095, the electron temperature is in the range $kT_e \sim 30$ – 90 keV (as inferred from the high-energy turn-off reported by Fuerst et al. 2018) and the Compton y -parameter is ~ 1.5 (see Section 2.2). Although the Corona temperature is fully compatible with that displayed by BH systems, this argument is not conclusive, since NSs can also reach such high values. The y -parameter, on the other hand, is well above the 0.9 boundary clearly favouring a BH accretor. Our y -value implies a Corona with an optical depth $\tau \sim 4$ ($kT_e \sim 50$ keV) for MAXI J1813–095, while an optical depth of ~ 2 is expected for NS systems at similar electron temperatures. In addition, it has also been shown that the equivalent width of the Fe reflection line is anti-correlated with the y -parameter (Gilfanov et al. 1999; Burke et al. 2017). It is worth mentioning that we measure an equivalent width of ~ 75 eV, which nicely sits in this relation when considering y -parameter ~ 1.5 .

The spectral parameters derived from the thermal component also suggest, although to a lesser extent, a BH accretor. The temperature (~ 0.2 keV) and the normalization ($> 10^3$) of the disc component, which contributes less than 10 per cent to the 0.5–10 keV flux, are fully consistent with values reported for BHs in the hard state (e.g. Reis et al. 2010; Armas Padilla et al. 2014; Shidatsu et al. 2014; Plant

⁶ Compton y -parameter is defined as $y = \frac{4kT}{mc^2} \text{Max}(\tau, \tau^2)$, where τ is the optical depth.

et al. 2015). NS systems accreting at low luminosities generally display hotter blackbody temperatures ($kT_{\text{bb}} \gtrsim 0.3$ keV) and lower normalizations ($< 10^3$), with this component typically contributing at the ~ 20 –50 per cent level (Degenaar et al. 2017; Sharma et al. 2018; Di Salvo et al. 2015). However, this fraction is anti-correlated with luminosity, and can be as low as $\lesssim 0$ –10 per cent at high luminosities ($L_X \gtrsim 10^{36}$ erg s $^{-1}$; Campana et al. 2014; Allen et al. 2015). Nevertheless, this lower thermal contribution would be accompanied by an increase on the black body temperature, from $kT_{\text{bb}} \sim 0.3$ –0.5 keV at $L_X \lesssim 10^{35}$ erg s $^{-1}$ to $kT_{\text{bb}} \sim 1$ –2 keV at $L_X \gtrsim 10^{36}$ erg s $^{-1}$ (Lin et al. 2007; Allen et al. 2015). Finally, our analysis of the rms-scaled spectrum suggests that in addition to the Comptonization component, the disc also contributes to the observed variability within the frequency range of 0.1–50 Hz. Disc variability has been reported in several BXRBs (e.g. Wilkinson & Uttley 2009; De Marco et al. 2015) and seems to be a characteristic feature of low luminosity hard states. All in all, the X-ray spectral characteristics of MAXI J1813–095 clearly favour a BH accretor.

4.1 On the optical counterpart and the distance to the source

Unfortunately, our optical spectra do not shed much light on the binary properties of MAXI J1813–095. We find that both outburst and quiescence data show stellar absorption features instead of broad emission lines. In Section 3.2, we explain that the absence of velocity shifts between outburst and quiescence, together with the evolution of the equivalent width of H α , strongly suggest that the optical emission from the system is dominated by that of an interloper star. This odd behaviour resembles that observed in other LMXBs, such as the prototypical NS transient Aql X-1, although in this case the accretion disc outshines the interloper in outburst (e.g. Mata Sánchez et al. 2017, and references therein). The faintness of the source ($i=19.7$ in quiescence) and the presence of strong Ca II features in absence of H Paschen components, clearly favour a spectral type G or K. Additionally, the equivalent width of the H α absorption line is correlated with the spectral type for cool, non-active stars (F to mid K; Scholz et al. 2007). The value derived from our quiescence data (2.7 Å) points towards a \sim G5 star. In addition to the PS1 catalog, an infrared counterpart to MAXI J1813–095 is present in the UKIDSS-DR6 Galactic Plane Survey (Lucas et al. 2008). The object is K=16.0 and its coordinates accurately match those of the optical counterpart. Adopting a G5–V spectral type we derive a distance of 3.4 kpc to the interloper star. To obtain this estimation we have neglected extinction effects and used the K absolute magnitude from Pecaut & Mamajek (2013).

Companion stars in LMXBs have typically G–K spectral types but these stars would not dominate the optical emission from the X-ray transient in outburst (e.g. Charles & Coe 2006). Even in the very atypical case of the BH transient V4641 Sgr with a \sim B9 donor, a strong H α emission component is detected in many spectra (Muñoz-Darias et al. 2018 for a recent study). On the other hand, the presence of an interloper star naturally explains the very odd outburst amplitude of only ~ 1 mag (see Corral-Santana et al. 2016 for typical outburst amplitudes in BH systems). Given the

late spectral type of the proposed interloper and the fact that LMXB accretion discs outshine their companions (of similar spectral types) by several orders of magnitude during outburst, we conclude that MAXI J1813–095 is most likely located further away than the interloper at a distance $\gtrsim 3$ kpc.

ACKNOWLEDGEMENTS

We thank the anonymous referee for constructive comments that improved the quality of this paper. We acknowledge support by the Spanish MINECO under grant AYA2017-83216-P. MAP’s research is funded under the Juan de la Cierva Fellowship Programme (IJC1-2016-30867). TMD and MAPT acknowledge support via a Ramon y Cajal Fellowship (RYC-2015-18148 and RYC-2015-17854, respectively). BDM acknowledges the Polish National Science Center for support under grant Polonez 2016/21/P/ST9/04025 and the European Commission for support under H2020-MSCA-IF-2017 action, Grant. No. 798726 BHmapping. We acknowledge the use of public data from the Swift data archive. *XMM-Newton* is an ESA science mission with instruments and contributions directly funded by ESA Member States and NASA. Based on observations made with the Gran Telescopio Canarias (GTC), instaled in the Spanish Observatorio del Roque de los Muchachos of the Instituto de Astrofísica de Canarias, in the island of La Palma. Based on observations collected at the European Southern Observatory under ESO programme 0100.D–0292(A). The authors are thankful to the GTC and VLT team that carried out the ToO observations. MOLLY software developed by T. R. Marsh is gratefully acknowledged.

REFERENCES

- Allen J. L., Linares M., Homan J., Chakrabarty D., 2015, *ApJ*, 801, 10
- Armas Padilla M., Degenaar N., Russell D. M., Wijnands R., 2013a, *MNRAS*, 428, 3083
- Armas Padilla M., Degenaar N., Wijnands R., 2013b, *MNRAS*, 434, 1586
- Armas Padilla M., Wijnands R., Altamirano D., Mendez M., Miller J. M., Degenaar N., 2014, *MNRAS*, 439, 3908
- Armas Padilla M., Ueda Y., Hori T., Shidatsu M., Muñoz-Darias T., 2017, *MNRAS*, 309, 290
- Armas Padilla M., Ponti G., De Marco B., Muñoz-Darias T., Haberl F., 2018, *MNRAS*, 473, 3789
- Arnaud K., 1996, in Jacoby G., Barnes J., eds, *Astronomical Society of the Pacific Conference Series Vol. 101, Astronomical Data Analysis Software and Systems V*. p. 17
- Belloni T. M., Motta S. E., Muñoz-Darias T., 2011, *Bulletin of the Astronomical Society of India*, 39, 409
- Burke M. J., Gilfanov M., Sunyaev R., 2017, *MNRAS*, 466, 194
- Burrows D. N., et al., 2005, *Space Sci. Rev.*, 120, 165
- Campana S., Brivio F., Degenaar N., Mereghetti S., Wijnands R., D’Avanzo P., Israel G. L., Stella L., 2014, *MNRAS*, 441, 1984
- Capitanio F., Belloni T., Del Santo M., Ubertini P., 2009, *MNRAS*, 398, 1194
- Casares J., Jonker P. G., 2014, *Space Sci. Rev.*, 183, 223
- Cepa J., et al., 2000. *International Society for Optics and Photonics*, p. 623
- Chambers K. C., et al., 2016, eprint arXiv:1612.05560

- Charles P. A., Coe M. J., 2006, in Lewin W., van der Klis M., eds., Vol. 39, In: Compact stellar X-ray sources. Edited by Walter Lewin & Michiel van der Klis.. Cambridge University Press, p. 690
- Corral-Santana J. M., Casares J., Muñoz-Darias T., Bauer F. E., Martínez-Pais I. G., Russell D. M., 2016, *A&A*, 587, A61
- De Marco B., Ponti G., Muñoz-Darias T., Nandra K., 2015, *MNRAS*, 454, 2360
- Degenaar N., Pinto C., Miller J. M., Wijnands R., Altamirano D., Paerels F., Fabian A. C., Chakrabarty D., 2017, *MNRAS*, 464, 398
- Di Salvo T., et al., 2015, *MNRAS*, 449, 2794
- Done C., Gierlinski M., Kubota A., 2007, *The Astronomy and Astrophysics Review*, 15, 1
- Dubus G., Kim R. S. J., Menou K., Szkody P., Bowen D. V., 2001, *ApJ*, 553, 307
- Fender R., Muñoz-Darias T., 2016, in and Haardt, F. and Gorini, V. and Moschella, U. and Treves A., Colpi M., eds., Vol. 905, Lect. Notes Phys.. Springer International Publishing, pp 65–100
- Fender R. P., Belloni T. M., Gallo E., 2004, *MNRAS*, 355, 1105
- Fuerst F., et al., 2018, The Astronomer’s Telegram, No. 11357, 11357
- Gehrels N., et al., 2004, *ApJ*, 611, 1005
- Gilfanov M., Churazov E., Revnivtsev M., 1999, *A&A*, 352, 182
- Gilfanov M., Churazov E., Revnivtsev M., 2000, *MNRAS*, 316, 923
- Greiner J., Sala G., Kruehler T., 2008, *atel*, 1577, 1
- Guainazzi M., Rodríguez-Pascual P., Smith M., 2014, Technical report, XMM-Newton Calibration Technical Note Spectral calibration accuracy in EPIC-pn fast modes History
- Homan J., Wijnands R., van der Klis M., Belloni T., van Paradijs J., Klein-Wolt M., Fender R., Méndez M., 2001, *ApJS*, 132, 377
- Jansen F., et al., 2001, *A&A*, 365, L1
- Jiménez-Ibarra F., et al., 2019, *MNRAS*, 484, 2078
- Kalogera V., Baym G., 1996, *ApJ*, 470, L61
- Kawase T., et al., 2018, The Astronomer’s Telegram, No. 11323, 11323
- Kirsch M., et al., 2004, in Hasinger G., Turner M., eds, Society of Photo-Optical Instrumentation Engineers (SPIE) Conference Series Vol. 5488, Society of Photo-Optical Instrumentation Engineers (SPIE) Conference Series. pp 103–114, doi:10.1117/12.549276
- Koljonen K. I. I., Russell D. M., Corral-Santana J. M., Armas Padilla M., Muñoz-Darias T., Lewis F., Coriat M., Bauer F. E., 2016, *MNRAS*, 460, 942
- Kubota A., Tanaka Y., Makishima K., Ueda Y., Dotani T., Inoue H., Yamaoka K., 1998, *PASJ*, 50, 667
- Lin D., Remillard R. A., Homan J., 2007, *ApJ*, 667, 1073
- Lucas P. W., et al., 2008, *MNRAS*, 391, 136
- Makishima K., Maejima Y., Mitsuda K., Bradt H. V., Remillard R. A., Tuohy I. R., Hoshi R., Nakagawa M., 1986, *ApJ*, 308, 635
- Mata Sánchez D., Muñoz-Darias T., Casares J., Jiménez-Ibarra F., 2017, *MNRAS Lett*, 464, L41
- Mata Sánchez D., et al., 2018, *MNRAS*, 481, 2646
- McClintock J. E., Remillard R. A., 2006, In: Compact stellar X-ray sources. Edited by Walter Lewin & Michiel van der Klis. Cambridge Astrophysics Series
- Mitsuda K., et al., 1984, *PASJ*, 36, 741
- Miyamoto S., Kimura K., Kitamoto S., Dotani T., Ebisawa K., 1991, *ApJ*, 383, 784
- Miyamoto S., Kitamoto S., Iga S., Negoro H., Terada K., 1992, *ApJ*, 391, L21
- Motta S., Muñoz-Darias T., Belloni T., 2010, *MNRAS*, 408, 1796
- Motta S. E., Rouco-Escorial A., Kuulkers E., Muñoz-Darias T., Sanna A., 2017, *MNRAS*, 468, 2311
- Muñoz-Darias T., Motta S., Belloni T. M., 2011, *MNRAS*, 410, 679
- Muñoz-Darias T., Fender R. P., Motta S. E., Belloni T. M., 2014, *MNRAS*, 443, 3270
- Muñoz-Darias T., et al., 2016, *Nature*, 534, 75
- Muñoz-Darias T., Torres M. A. P., Garcia M. R., 2018, *MNRAS*, 479, 3987
- Pecaut M. J., Mamajek E. E., 2013, *ApJS*, 208, 9
- Plant D. S., Fender R. P., Ponti G., Muñoz-Darias T., Coriat M., 2015, *A&A*, 573, A120
- Poutanen J., Svensson R., 1996, *ApJ*, 470, 249
- Price-Whelan A. M., et al., 2018, *AJ*, 156, 123
- Rau A., 2018, The Astronomer’s Telegram, No. 11332, 11332
- Reis R. C., Fabian A. C., Miller J. M., 2010, *MNRAS*, 402, 836
- Rhoades C., Ruffini R., 1974, *Phys. Rev. Lett.*, 32, 324
- Robitaille T. P., et al., 2013, *A&A*, 558, A33
- Russell T. D., Miller-Jones J. C. A., Sivakoff G. R., Tetarenko A. J., Collaboration J. X., 2018, The Astronomer’s Telegram, No. 11356, 11356
- Scholz A., Coffey J., Brandeker A., Jayawardhana R., 2007, *ApJ*, 662, 1254
- Shakura N. I., Sunyaev R. A., 1973, *A&A*, 24, 337
- Sharma R., Jaleel A., Jain C., Pandey J. C., Paul B., Dutta A., 2018, *MNRAS*, 481, 5560
- Shidatsu M., et al., 2014, *ApJ*, 789, 100
- Smak J., 1969, *Acta Astronomica*, 19, 155
- Strüder L., et al., 2001, *A&A*, 365, L18
- Sunyaev R., Titarchuk L., 1989, in Hunt J., Battrick B., eds., Two Topics in X-Ray Astronomy, Volume 1: X Ray Binaries. Volume 2: AGN and the X Ray Background. ESA Special Publication, pp 627–631
- Turner M., et al., 2001, *A&A*, 365, L27
- Uttley P., Cackett E. M., Fabian A. C., Kara E., Wilkins D. R., 2014, *The Astronomy and Astrophysics Review*, 22, 72
- Verner D., Ferland G., Korista K., Yakovlev D., 1996, *ApJ*, 465, 487
- Vernet J., et al., 2011, *A&A*, 536, A105
- Wilkinson T., Uttley P., 2009, *MNRAS*, 397, 666
- Wilms J., Allen A., McCray R., 2000, *ApJ*, 542, 914
- Yamada S., Makishima K., Done C., Torii S., Noda H., Sakurai S., 2013, *PASJ*, 65, 80
- Zdziarski A., Johnson W., Magdziarz P., 1996, *MNRAS*, 283, 193
- Zycki P. T., Done C., Smith D. A., 1999, *MNRAS*, 309, 561
- van der Klis M., 2006, *Adv. Sp. Res.*, 38, 2675

This paper has been typeset from a $\text{\TeX}/\text{\LaTeX}$ file prepared by the author.